Experimentally Validated Simulations of Blind Hole Drilling in 3D Woven Carbon/Epoxy Composite with Processing-Induced Residual Stresses

ARTURO LEOS, KOSTIANTYN VASYLEVSKYI,
IGOR TSUKROV, TODD GROSS and BORYS DRACH

ABSTRACT

Manufacturing-induced residual stresses in carbon/epoxy 3D woven composites arise during cooling after curing due to a large difference in the coefficients of thermal expansion between the carbon fibers and the epoxy matrix. The magnitudes of these stresses appear to be higher in composites with high through-thickness reinforcement and in some cases are sufficient to lead to matrix cracking.

This paper presents a numerical approach to simulation of development of manufacturing-induced residual stresses in an orthogonal 3D woven composite unit cell using finite element analysis. The proposed mesoscale modeling combines viscoelastic stress relaxation of the epoxy matrix and realistic reinforcement geometry (based on microtomography and fabric mechanics simulations) and includes imaging-informed interfacial (tow/matrix) cracks. Sensitivity of the numerical predictions to reinforcement geometry and presence of defects is discussed. To validate the predictions, blind hole drilling is simulated, and the predicted resulting surface displacements are compared to the experimentally measured values.

The validated model provides an insight into the volumetric distribution of residual stresses in 3D woven composites. The presented approach can be used for studies of residual stress effects on mechanical performance of composites and strategies directed at their mitigation.

Arturo Leos, Borys Drach: New Mexico State University, Department of Mechanical and Aerospace Engineering, 1040 S. Horseshoe Str., Las Cruces, NM 88003, U.S.A.
Kostiantyn Vasylevskyi, Igor Tsukrov, Todd Gross: University of New Hampshire, Department of Mechanical Engineering, 33 Academic Way, Durham, NH 03824, U.S.A.

INTRODUCTION

Residual stresses develop in resin matrix woven composite materials during manufacturing. Depending on the types of materials used in a given composite system and architecture of the reinforcement, these stresses may reach high magnitudes and have significant effects on the composite's performance. In carbon/epoxy fiber-reinforced composites most of residual stresses are assumed to develop during cooling from curing to room temperature due to a large mismatch in the coefficients of thermal expansion between the matrix and the reinforcement phases.

To study the effects of the residual stresses on mechanical properties of composite parts and develop approaches for the stress mitigation, distribution of these stresses must be known. However, inferring volumetric distribution of residual stresses directly from experimental measurements, such as blind hole drilling, is not possible due to heterogeneity of composites and nonlinear material behavior of their constituents. As a result, numerical approaches are required for modeling of distribution of manufacturing-induced residual stresses as a function of processing parameters.

In our previous publications, we used numerical modeling to predict volumetric distribution of residual stresses in ply-to-ply 3D woven composites with low levels of orthogonal reinforcement [1]. The results were successfully validated by comparing simulated and experimental surface displacements resulting from blind hole drilling. In [2], we explored application of the previously developed numerical approach to the one-by-one orthogonally reinforced 3D woven composite. It was found that for the best predictions, viscoelastic relaxation of the composite matrix and microstructural defects, i.e., matrix-tow debonding need to be incorporated in the numerical modeling.

In this work, we employ finite element analysis to zero in on the best numerical approach to simulation of complete volumetric distribution of processing-induced residual stresses in an orthogonal 3D woven composite model. The studies are conducted on the mesoscale (scale of woven architecture, see Figure 1a). In our previous work [2], we examined effects of the matrix material constitutive model and presence of defects on surface displacements following blind hole drilling. This publication builds on [2] by adding an analysis of sensitivity of residual stresses to variations in the reinforcement geometry. For this purpose, two models are compared, one obtained directly from microtomography data, and another generated using fabric mechanics simulations. Finally, the effects of presence of defects are discussed for both models. Validity of all numerical results is evaluated by comparing predicted and experimentally obtained displacements arising from blind hole drilling in the presence of residual stresses developed for each geometric model (microtomography-based vs generated) and defect configuration (undamaged vs models with tow/matrix debonding).

FINITE ELEMENT MODELS

All numerical analyses presented in this paper were performed using the commercial general purpose finite element (FE) package MSC Marc Mentat.

Geometry

The considered 3D woven composite has the "one-by-one orthogonal" reinforcement architecture shown in Figure 1a. The reinforcement is composed of ten layers of interwoven fiber bundles (tows) aligned along mutually orthogonal directions (warp and weft) with through-thickness tows binding all layers. The unit cell dimensions are $5.08 \times 5.08 \times 3.92\ mm^3$.

Two finite element models of the 3D woven configuration are considered in this paper. The first model uses geometry extracted directly from microtomography imaging of an actual composite panel and is referred to in the text as the "μCT model". The second model is based on geometry generated using fabric mechanics simulations performed in the DFMA software as discussed below and is referred to in this paper as the "DFMA model".

To generate the μCT model, a quarter of the symmetric "one-by-one orthogonal" composite unit cell (smallest repeating portion of the composite) was extracted from μCT data of a composite panel. The image sequence of the quarter unit cell was then segmented to isolate individual tows. Segmentation was performed in ImageJ [3] by outlining tow cross-sections manually in μCT sections approximately 100 μm apart. Tow profiles between the sections were interpolated. A small gap was introduced between adjacent tows to eliminate overlapping of tow geometry and enable conformal meshing of the composite unit cell. Point clouds extracted from the segmented μCT data were then processed in Rhino [4] to generate non-uniform rational basis spline (NURBS) surfaces of individual tows. Tow surfaces were meshed in MSC Patran with three-node triangular elements; then the surface mesh of all tows comprising the composite reinforcement was mirrored to get a complete unit cell and converted to volumetric ten-node tetrahedral meshes in MSC Mentat. The final mesh of a single unit cell with the reinforcement geometry shown in Figure 1b consisted of 1,667,549 nodes and 1,226,616 elements (matrix + reinforcement). A more detailed description of the geometry preparation procedure is presented in [5], [6].

In the case of the second model, geometry of the reinforcement was developed using the Digital Fabric Mechanic Analyzer (DFMA, Kansas State University) [7], [8]. DFMA uses basic reinforcement information including number of warp and weft columns, weave pattern, column spacing and tow cross-sectional area as inputs for the modeling process. During a fabric mechanics simulation, each tow is subdivided into bundles of "digital chains" and is subjected to tensile forces to simulate the weaving process. The final arrangement of the digital chains is converted to homogeneous solid models of tows. Before simulation-ready meshes are generated from DFMA output, the geometry is processed using custom scripts to remove geometric incompatibilities in the form of tow interpenetrations, see examples of implementation of similar methods in [9], [10]. The final mesh of a single unit cell with reinforcement geometry shown in Figure 1c consisted of 826,601 nodes and 597,448 ten-node tetrahedral elements (matrix + reinforcement). A detailed description of the modeling process is provided in [11], [12]. In addition, the previously developed models [12] were modified to remove a thin epoxy resin layer covering top and bottom of the unit cell to better represent the actual composite configuration. The layer had previously been introduced to avoid cutting across tows near the composite panel surfaces and make meshing easier. For a more detailed discussion of this modification, see [2].

Influence of structural defects in the form of tow/matrix debonding on surface displacements following blind hole drilling in the presence of residual stresses is investigated by analyzing defect-free and cracked μCT and DFMA models. The tow/matrix cracks were observed on the concave sides of most binder tows in two microtomography datasets obtained from two composite specimens. The cracks along with their average dimensions are shown in Figure 2a and Figure 2b. To model the defects numerically, a 0.01-mm gap was introduced between the binder tows and the matrix in the "cracked" finite element models. The shape of one of the cracks is illustrated via highlighted faces on a DFMA model's binder tow shown in Figure 2c.

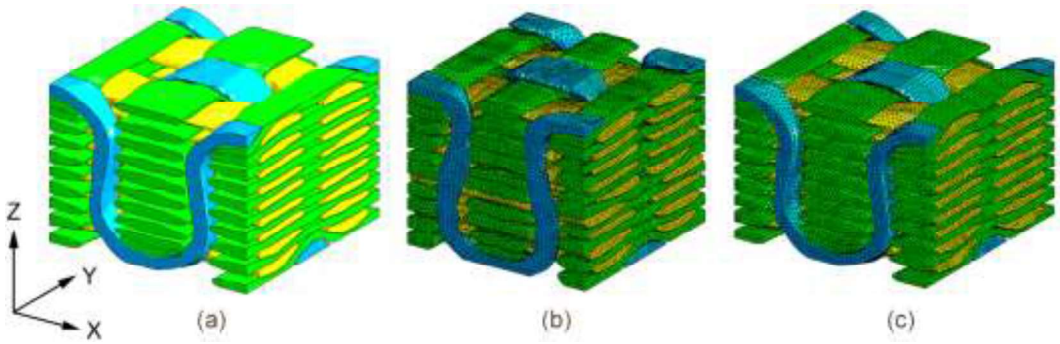

Figure 1. Reinforcement of the one-by-one orthogonal 3D woven composite (matrix is hidden):
(a) weave architecture showing warp (green), weft (yellow) and binder (blue) tows;
(b) mesh of the reinforcement in the μCT model; (c) mesh of the reinforcement in the DFMA model.

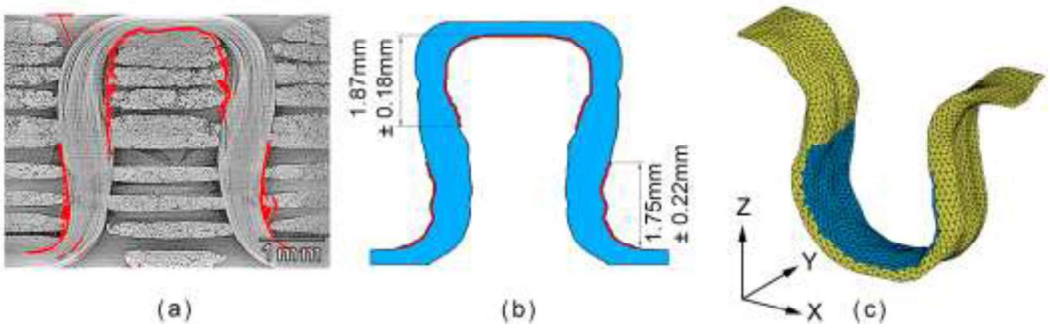

Figure 2. Interface cracks observed in the considered 3D woven composite:
(a) illustration of the cracks in microtomography imaging; (b) average dimensions of the cracks;
(c) crack faces highlighted on a DFMA model's binder tow.

Material Properties

The matrix phase is HEXCEL RTM6 epoxy resin, and the reinforcement tows consist of 12,000 of IM7 carbon fibers each. The epoxy is modeled as a viscoelastic material based on the measurements presented in [13]. Viscoelasticity is implemented numerically using Prony Series with a short-term Young's modulus $E_m = 4.88\ GPa$ and a Poisson's ratio $\nu_m = 0.359$. The following time and temperature dependent functions are used for shear ($G(t,T)$) and bulk ($K(t,T)$) moduli

$$G(t,T) = G_\infty + \sum_{k=1}^{N} G_k e^{\frac{-ta(T)}{\tau_{Gk}}} \quad (1)$$

$$K(t,T) = K_\infty + \sum_{k=1}^{N} K_k e^{\frac{-ta(T)}{\tau_{Kk}}} \quad (2)$$

where t is time (s), T is temperature ($°C$), $\tau_{...k}$ is relaxation time of the Prony series term k, G_k and K_k are the stiffnesses in the Prony series term k, G_∞ and K_∞ are the long term stiffnesses, N is the order of the series, and

$$\log\big(a(T)\big) = \frac{C_1(T-T_{ref})}{C_2+(T-T_{ref})} \quad (3)$$

is the Williams-Landel-Ferry shift function with coefficients $C_1 = 1790.35$ and $C_2 = 14028.2\ °C$, and reference temperature $T_{ref} = 100°C$. The coefficients used to fit Prony series to the experimental data are given in TABLE I [14]. Finally, the coefficient of thermal expansion (CTE) is input as a linear function of temperature with values $\alpha_{O°C} = 5 \cdot 10^{-5}/°C$ at 0°C and $\alpha_{180°C} = 6.89 \cdot 10^{-5}/°C$ at 180°C [15].

TABLE I. Prony series coefficients used to model matrix viscoelasticity [14].

	Deviatoric Behavior		**Volumetric Behavior**	
Term (k)	**Relaxation Time (τ_{Gk})**	**Shear Constant (G_k)**	**Relaxation Time (τ_{Kk})**	**Bulk Constant (K_k)**
1	3.35E-09	811.68	3.20E-09	2811.27
2	1.65E-06	46.03	1.64E-06	139.26
3	1.17E-03	23.80	1.18E-03	71.28
4	3.56E-01	40.41	3.56E-01	121.02
5	1.32E+02	51.06	1.31E+02	153.22
6	1.06E+05	53.33	1.06E+05	160.23
7	5.65E+07	65.95	5.66E+07	197.82
8	4.47E+10	86.21	4.48E+10	258.79
9	3.24E+12	56.66	3.24E+12	170.61
10	1.84E+13	153.06	1.84E+13	458.23

Tows are modeled as homogenized unidirectional composites with 80% fiber volume fraction and transversely isotropic temperature dependent thermoelastic effective properties. Homogenization was previously performed in [14] with effective properties given in TABLE II and Figure 3. Note that direction 1 coincides with the longitudinal fiber direction and $E_2 = E_3$ because of transverse isotropy.

TABLE II. Homogenized temperature independent thermoelastic properties of the tows [14], [15].

Material	E_1 (GPa)	$\alpha_1(\frac{1}{°C})$	$\alpha_{2,3}(\frac{1}{°C})$	v_{12}	v_{23}
RTM6 epoxy + IM7 carbon fibers ($V_f = 80\%$)	221	$-2.42 \cdot 10^{-7}$	$2.10 \cdot 10^{-5}$	0.35	0.35

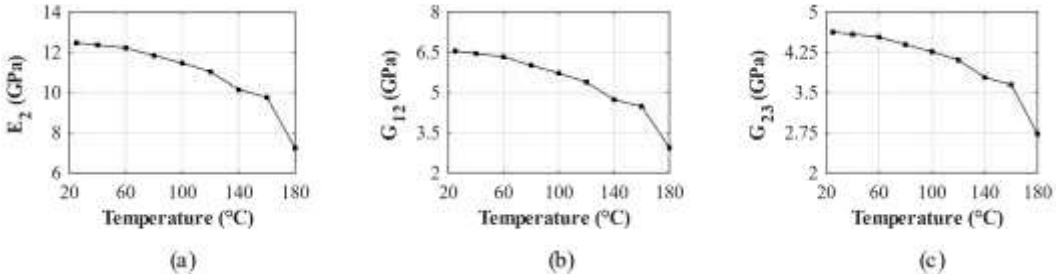

Figure 3. Homogenized temperature dependent elastic properties of the tows [14]: (a) transverse Young's modulus; (b) axial shear modulus; (c) in-plane shear modulus

Cooling simulation

Processing-induced residual stresses are predicted numerically in models with and without tow/matrix debonding discussed in the Geometry section and shown in Figure 2. The residual stresses are assumed to arise primarily during cooling from curing to room temperature due to a mismatch in the coefficients of thermal expansion between carbon fibers and epoxy matrix. Cooling simulations are performed by applying a temperature drop from 165°C to 25°C over 1700 seconds (approximately at a rate of 5°C/min). The prescribed temperature condition is applied uniformly over all elements.

Periodic boundary conditions (PBCs) are applied to the outer surfaces of the finite element model in the warp (x) and weft (y) directions using the approach described in [15]. The model represents the total thickness of the composite in the binder (z) direction and therefore periodic boundary conditions in that direction are not needed.

Blind Hole Drilling

To minimize the boundary effects and propagation of displacements following blind hole drilling to the periodic boundary conditions, unit cells shown in Figure 1 were duplicated to create a four-cell configuration. In addition, padding with homogeneous material properties was added around the portion of the material with explicit reinforcement geometry, see Figure 4. In such a configuration, all hole drilling locations discussed later in this paper are sufficiently removed from the boundaries.

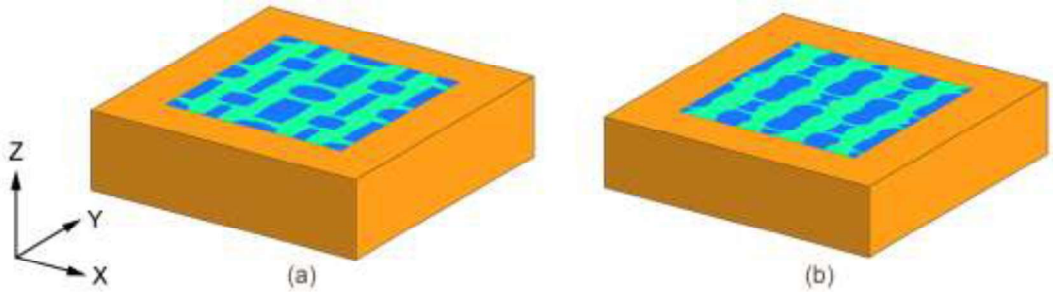

Figure 4. FEA models consisting of four unit cells surrounded by padding elements with homogenized properties: (a) μCT-based model; (b) DFMA-based model.

Blind hole drilling simulations were performed by importing cooling simulation results into the four-unit cell model with padding elements as the initial state of stress, and subsequently deactivating the elements corresponding to the drilled hole. Three holes at different locations within the composite unit cell (see Figure 5) were drilled numerically. The resulting surface displacements were validated against the experimental data collected for the same composite material and hole locations as presented in [16]. Note that drilling of each hole was simulated separately to avoid interaction of displacement fields following the drilling. PBCs in the blind hole drilling simulations are applied in the same manner as discussed before.

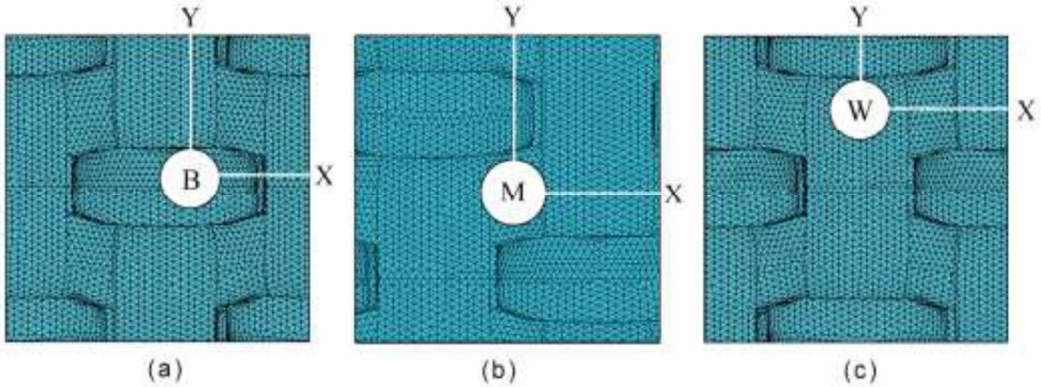

Figure 5. Locations of the holes drilled numerically (locations match experiments presented in [16]): (a) binder tow hole; (b) matrix hole; (c) weft tow hole.

RESULTS AND DISCUSSION

This section discusses the distributions and the effects of residual stresses developed in the μCT- and DFMA-based models shown in Figure 4 due to cooling after curing. The results are presented in the form of contour plots of residual stresses for the tow and matrix phases separately, and plots of surface displacements arising from drilling of blind holes in the locations identified in Figure 5. Obtaining full-field distribution of residual stresses within an actual composite seems to be out of reach given existing experimental methods, so direct validation of the simulated stresses is not possible. Instead, the numerical results are validated by comparing experimentally

observed and predicted surface displacements due to blind hole drilling at three locations. It is assumed that if a good agreement is observed in this validation, the predicted distribution of residual stresses is representative of the actual distribution.

The surface displacement results are presented in the form of path plots of warp (u_X) and weft (u_Y) displacements along X and Y axes, see Figure 5 for an illustration of the coordinate system.

Results for Defect-Free Models

First, perfect bonding between the matrix and the tows was assumed. Surface displacements resulting from drilling blind holes in three locations in the two FEA models, μCT- and DFMA-based, along with the experimental results are presented in Figure 6.

Magnitudes of displacements near the hole edges are overpredicted by both models with the DFMA-based model's predictions being closer to the experimental results. At the same time, the overall trends in the experimental surface displacement plots are generally reproduced well by the numerical models. Notable exceptions are warp displacements around the binder tow hole and weft displacements around the matrix hole. In the former case, even the signs of displacements are not predicted correctly by the models. In particular, the experimental results point to the binder hole opening in the warp (X) direction – displacements are negative to the left of the hole and positive to the right of the hole. In contrast, the μCT-based model predicts closure of the hole following blind hole drilling, and the DFMA-based model predicts shifting of the entire hole to in the positive X direction.

The substantial difference in the predictions from the two models is explained by differences in the μCT- and DFMA-derived reinforcement geometry. Comparing shapes of the tows shown in Figure 1b and Figure 1c, the binder tow, for example, is thicker and has a more pronounced omega-shaped path in the μCT-based architecture than the same tow in the DFMA model. In addition, all warp and weft tows appear to be wider in the DFMA model. At the same time, the DFMA model appears to lead to better predictions compared to the μCT model. This is surprising because the μCT geometry obtained directly from imaging is expected to be the best virtual representation of the actual composite reinforcement. This disconnect may potentially be explained by the defects in the dataset from which μCT model was constructed – the entire unit cell in the composite specimen appears to be skewed. To preserve the periodicity, a quarter of the unit cell was extracted and mirrored. As a result, one of the two columns of the weft tows and one of two binder tows are much narrower than the rest.

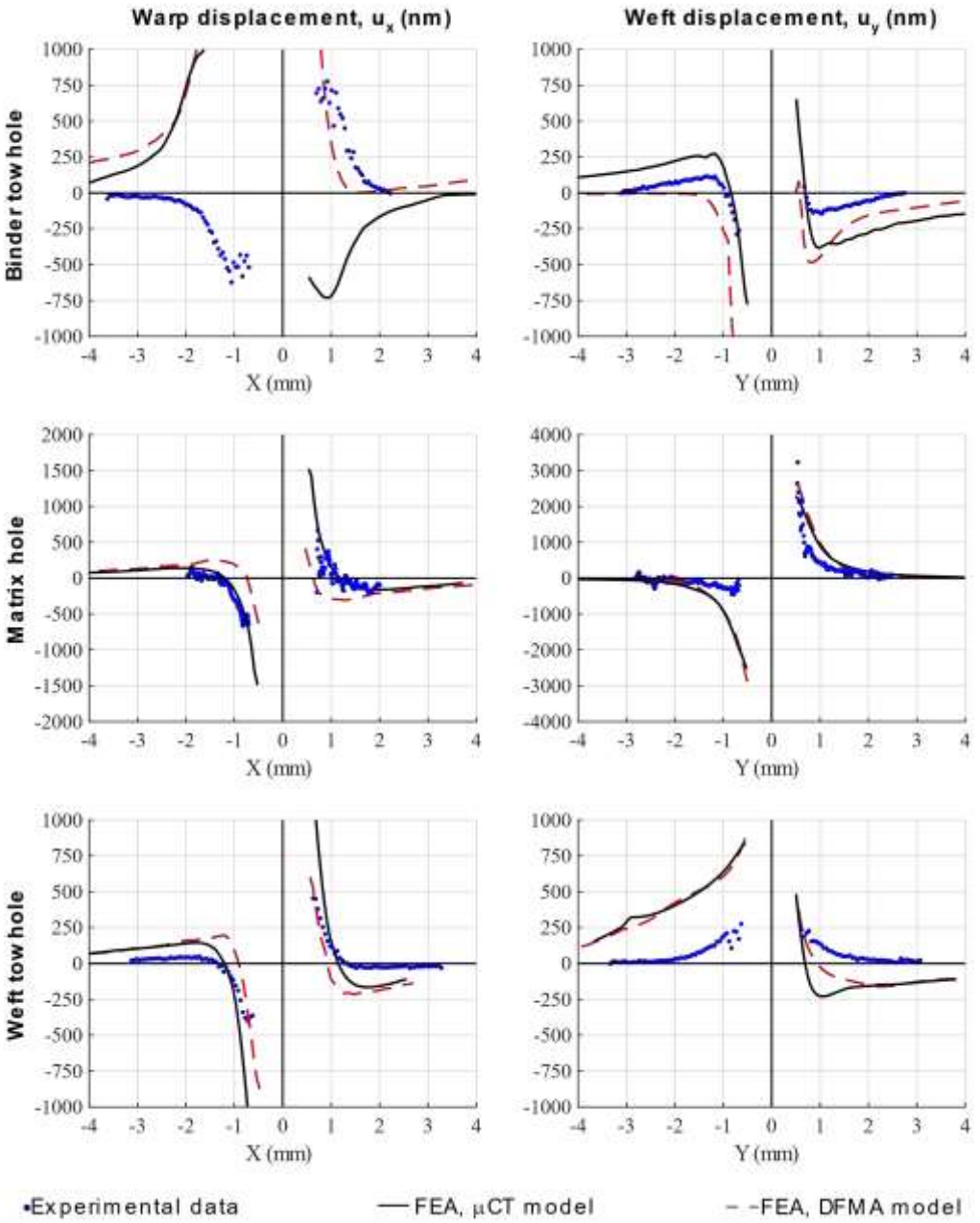

Figure 6. Comparison of experimental and numerical surface displacements in the warp (left) and weft (right) directions for the binder tow, matrix and weft tow holes. Numerical results are shown for the μCT and DFMA models without microcracking.

Results for Models with Imaging-Informed Interface Cracks

In an effort to improve the numerical predictions of the processing-induced residual stresses and consequently predictions of the surface displacements following blind hole drilling, microstructural defects in the form of binder tow/matrix interface cracks are introduced before the cooling simulation. Dimensions of the cracks are informed by microtomography imaging as discussed in the Geometry section of this paper.

The effects of introducing interface cracks on the predictions of surface displacements following hole drilling can be seen in Figure 7. Most notably, the trends in the numerical predictions for the warp displacements near the binder tow hole are now in agreement between both numerical models and the experimental results. In addition, introduction of cracks significantly lowers magnitudes of weft displacements around the binder and the weft tow holes. At the same time, virtually no changes are observed in either surface displacement component around the matrix hole and the warp displacements around the weft hole.

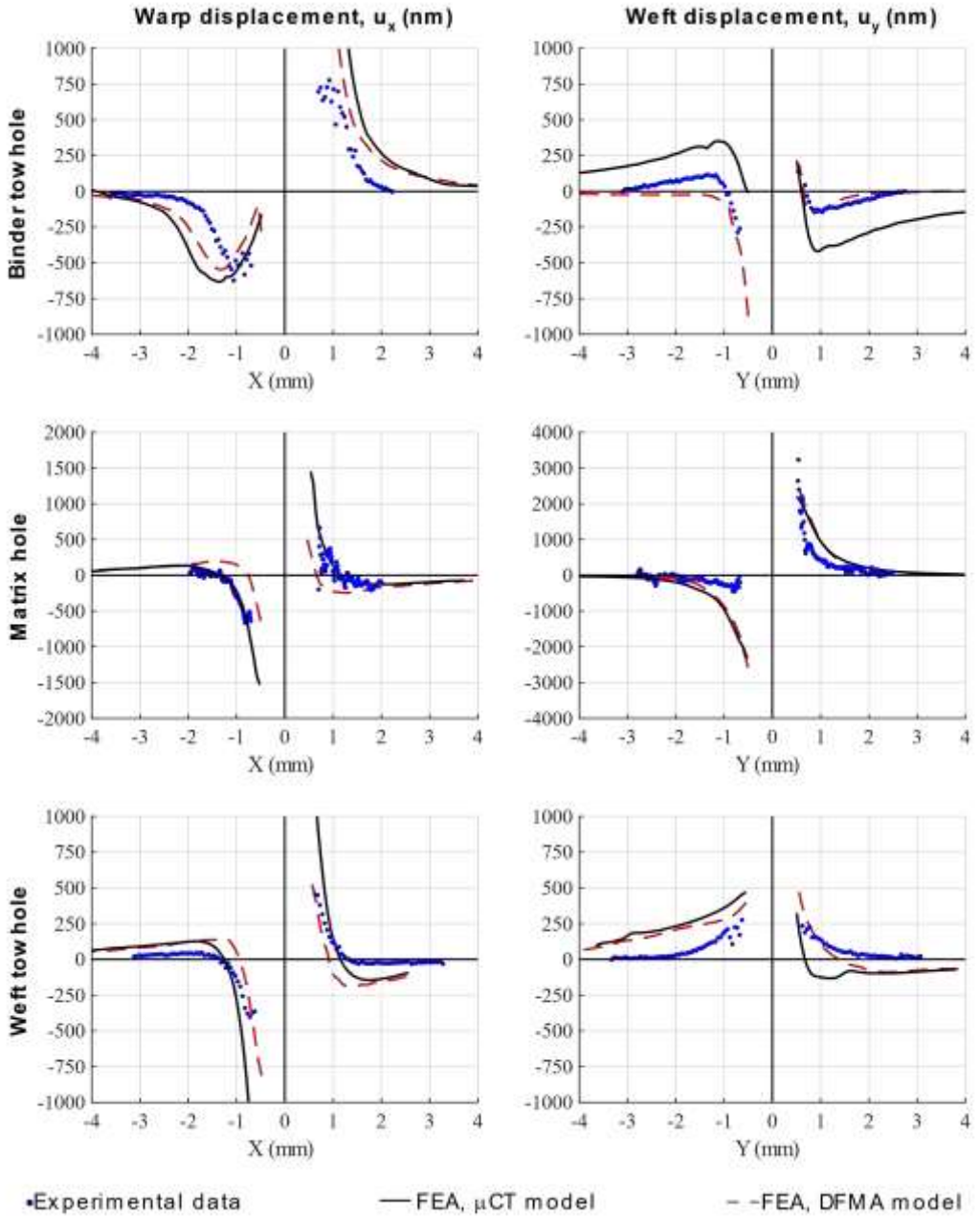

Figure 7. Comparison of experimental and numerical surface displacements in the warp (left) and weft (right) directions for the binder tow, matrix and weft tow holes. Numerical results are shown for the μCT and DFMA models with microcracking.

As in the case of models without cracks, magnitudes of displacements predicted by the DFMA-based model are closer to the experimental, although several significant discrepancies remain. Warp displacements to the right of the binder hole, weft displacements below the binder hole, and weft displacements below the matrix hole are all significantly overpredicted by the DFMA-based model.

In the case of the matrix hole, the near-zero experimental displacements below the hole can be explained by the geometric configuration of the composite panel – the path along which experimental displacements are sampled crosses the nearby exposed binder tow which develops tensile residual stresses transverse to the tow's longitudinal axis. The residual stresses in the tow are lower in magnitude compared to the matrix pocket around it. In contrast, the numerical sample path below the hole is contained to matrix only. Experimental and numerical sample paths above the hole are both contained to matrix only and show good agreement. Stress distributions within the matrix and the tow phases are discussed below.

In the case of the binder tow hole, the overpredictions may potentially be explained by the limitations of the electronic speckle pattern interferometry (ESPI) technique that was used to obtain the experimental validation displacement data ([12], [17]). Namely, the technique results in a very dense collection of fringes in the locations with steep displacements gradients. In some cases, the pattern is so dense that individual fringes cannot be resolved and the displacement data in such locations cannot be retrieved. Numerical predictions for the warp displacements to the right and weft displacements below the binder hole point to steep gradients in those locations, so it appears that the experimental data near the hole edges is simply incomplete which results in what appears to be lower magnitudes when compared to the numerical predictions.

The final distributions of predicted residual stress components resulting from cooling after curing in the μCT and DFMA models with cracks are shown in Figure 8 and Figure 9, respectively. In both models, warp and weft stresses in the matrix are tensile, which is a result of a much higher coefficient of thermal expansion of the epoxy matrix compared to the effective CTEs of the tows in the longitudinal direction. With the transverse response of the tows being dominated by the matrix, transverse stresses in the tows are also tensile. On the other hand, the CTE mismatch leads to significant compressive longitudinal stresses in the tows.

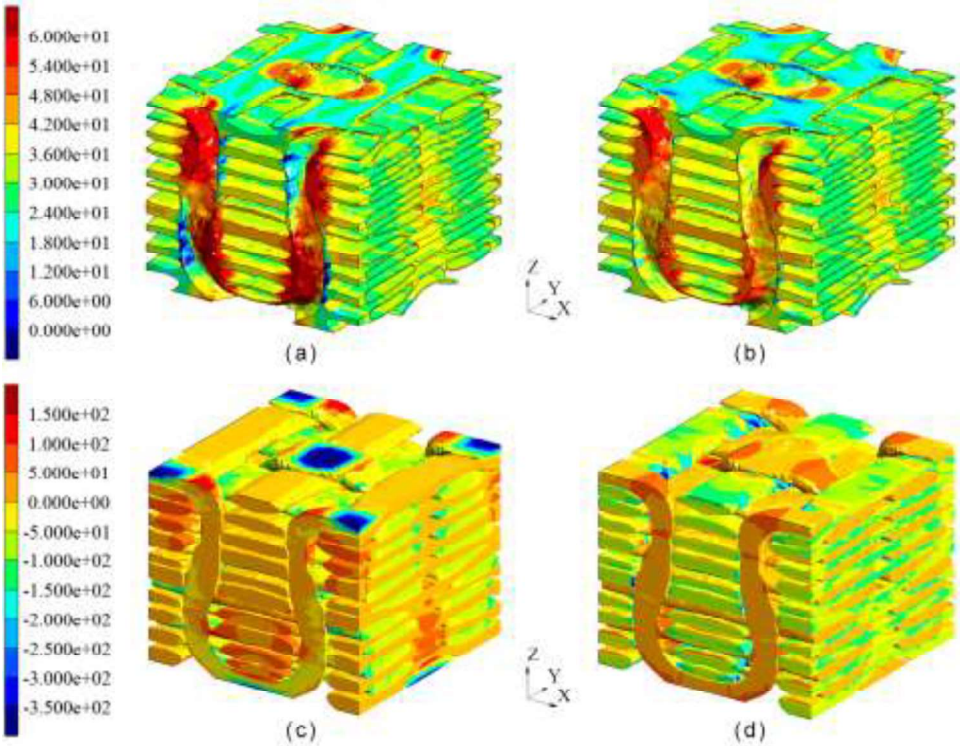

Figure 8. Distribution of stresses following cooling after curing in the μCT model with microcracking, MPa: (a) warp component (X) in the matrix; (b) weft component (Y) in the matrix; (c) warp component (X) in the tows; (d) weft component (Y) in the tows.

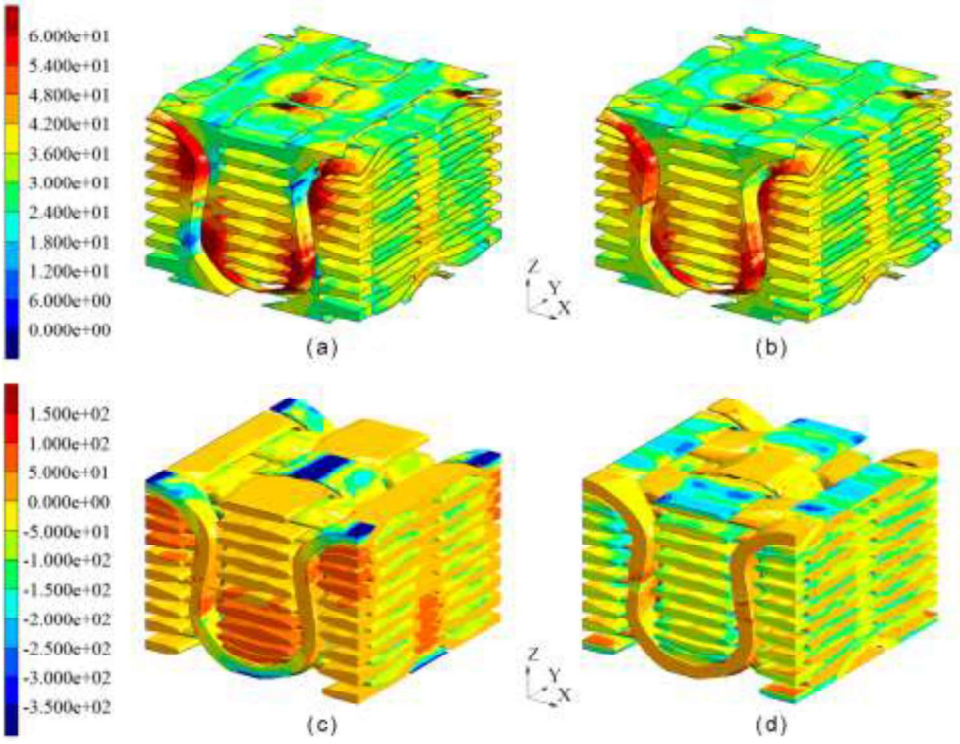

Figure 9. Distribution of stresses following cooling after curing in the DFMA model with microcracking, MPa: (a) warp component (X) in the matrix; (b) weft component (Y) in the matrix; (c) warp component (X) in the tows; (d) weft component (Y) in the tows.

CONCLUSIONS

This paper presents a nonlinear mesoscale finite element approach for predicting processing-induced residual stresses in carbon/epoxy 3D woven composites. The numerical results are validated by comparing predicted and experimentally measured surface displacements resulting from blind hole drilling.

After comparing predictions from numerical models based on two different reinforcement architectures (one obtained from microtomography, μCT, and another generated via fabric mechanics simulations, DFMA), we conclude that residual stresses are sensitive to reinforcement geometry. Differences are observed in the hole drilling displacements and distributions of stress components in the matrix and the tow phases.

In this comparison, the model with generated geometry resulted in better predictions of surface displacements than the model with imaging-based geometry. This surprising observation can be explained by imperfections in the reinforcement architectures found in the available composite panels – entire vertical stacks of tows appear to be skewed possibly as a result of compression during resin transfer molding.

In addition, comparison of results from models with and without cracks on the binder tow/matrix interface highlights how much defects alleviate residual stresses. For accurate predictions of the processing-induced stresses, it is important that defects are incorporated in numerical modeling either through progressive damage analysis or at least by introducing them before residual stress accumulation, i.e. cooling after curing in the case of curing at elevated temperatures.

Despite the remaining discrepancies between predictions by the DFMA model and experimental results, which are explained by differences in the reinforcement geometry and limitations of the imaging method used for measuring surface displacements, the proposed approach is very promising. Using our methodology, complete volumetric distributions of residual stresses can now be analyzed for sensitivity to processing conditions (e.g. curing temperature, cooling rate etc.), material properties (e.g. viscoelastic relaxation of the matrix material), and reinforcement geometry features (e.g. number of layers bound by a binder tow in a single unit cell). These analyses will enable a modeling-based search for strategies aimed at mitigation of residual stresses in high performance 3D woven composites, and studies of the effects of these stresses on the composites' mechanical behavior and service life.

ACKNOWLEDGEMENTS

This material is based upon work supported by the National Science Foundation under Grant No. CMMI-1662098.

REFERENCES

[1] K. Vasylevskyi, I. Tsukrov, H. Buntrock, T. Gross, and B. Drach, "Implementation of Numerical Models to Evaluate Intrinsic Residual Stresses in 3D Woven Composites by Blind Hole Drilling Tests," in *American Society for Composites 2020*, 2020.

[2] A. Leos, K. Vasylevskyi, I. Tsukrov, T. Gross, and B. Drach, "Evaluation of Process-Induced Residual Stresses in Orthogonal 3D Woven Composites by Hole Drilling and Nonlinear Finite Element Modeling," *Compos. Part A Appl. Sci. Manuf.*

[3] C. A. Schneider, W. S. Rasband, and K. W. Eliceiri, "NIH Image to ImageJ: 25 years of image analysis," *Nat. Methods*, vol. 9, no. 7, pp. 671–675, Jul. 2012.

[4] "Rhinoceros 6." Robert McNeel & Associates, Seattle, WA, USA.

[5] A. Ewert, "M.S. Thesis: Predicting the overall response of an orthogonal 3D woven composite using simulated and tomography-derived geometry," New Mexico State University, 2019.

[6] A. Ewert, B. Drach, K. Vasylevskyi, and I. Tsukrov, "Predicting the overall response of an orthogonal 3D woven composite using simulated and tomography-derived geometry," *Compos. Struct.*, vol. 243, no. October 2019, p. 112169, 2020.

[7] G. Zhou, X. Sun, and Y. Wang, "Multi-chain digital element analysis in textile mechanics," *Compos. Sci. Technol.*, vol. 64, no. 2, pp. 239–244, Feb. 2004.

[8] L. Huang, Y. Wang, Y. Miao, D. Swenson, Y. Ma, and C.-F. Yen, "Dynamic relaxation approach with periodic boundary conditions in determining the 3-D woven textile micro-geometry," *Compos. Struct.*, vol. 106, pp. 417–425, Dec. 2013.

[9] A. Drach, B. Drach, and I. Tsukrov, "Processing of fiber architecture data for finite element modeling of 3D woven composites Dedicated to Professor Zdeněk Bittnar in occasion of his 70th birthday.," *Adv. Eng. Softw.*, vol. 72, pp. 18–27, 2014.

[10] B. Drach, A. Drach, I. Tsukrov, M. Penverne, and Y. Lapusta, "Finite element models of 3D woven composites based on numerically generated micro-geometry of Reinforcement," in *Proceedings of the American Society for Composites - 29th Technical Conference, ASC 2014; 16th US-Japan Conference on Composite Materials; ASTM-D30 Meeting*, 2014.

[11] A. Drach, B. Drach, and I. Tsukrov, "Processing of fiber architecture data for finite element modeling of 3D woven composites," *Adv. Eng. Softw.*, vol. 72, pp. 18–27, Jun. 2014.

[12] K. Vasylevskyi, I. Tsukrov, B. Drach, H. Buntrock, and T. Gross, "Identification of process-induced residual stresses in 3D woven carbon/epoxy composites by combination of FEA and blind hole drilling," *Compos. Part A Appl. Sci. Manuf.*, vol. 130, 2020.

[13] C. Brauner, T. Block, H. Purol, and A. Herrmann, "Microlevel manufacturing process simulation of carbon fiber/epoxy composites to analyze the effect of chemical and thermal induced residual stresses," *J. Compos. Mater.*, vol. 46, no. 17, pp. 2123–2143, 2012.

[14] H. Galdino da Silva, "M.S. Thesis: 3D woven composites: two-step homogenization of architectures with high crimp ratios, and analysis of residual stresses and their effects," New Mexico State University, 2019.

[15] B. Drach, I. Tsukrov, A. Trofimov, T. Gross, and A. Drach, "Comparison of stress-based failure criteria for prediction of curing induced damage in 3D woven composites," *Compos. Struct.*, vol. 189, pp. 366–377, Apr. 2018.

[16] K. Vasylevskyi, I. Tsukrov, B. Drach, H. Buntrock, and T. Gross, "Identification of process-induced residual stresses in 3D woven carbon/epoxy composites by combination of FEA and blind hole drilling," *Compos. Part A Appl. Sci. Manuf.*, vol. 130, no. July 2019, p. 105734, 2020.

[17] T. Gross, H. Buntrock, I. Tsukrov, B. Drach, K. Vasylevskyi, and N. Chagnon, "Measurement of Intrinsic Residual Stresses in 3D Woven Composites Using Measurement of the Displacement Fields from Hole Drilling by Electronic Speckle Pattern Interferometry and Digital Image Correlation," in *American Society for Composites 2018*, 2018.